

Simulation of fluid–flexible structure interaction

Wei-Xi Huang¹ & Hyung Jin Sung¹

¹Department of Mechanical Engineering, KAIST, Korea

Keywords: Fluid–structure interaction, Immersed boundary method, Flexible body, Numerical simulation

Abstract: Systems involving flexible bodies interacting with surrounding fluid flow are commonplace, but are challenging to model numerically on account of their complex geometries and freely moving boundaries. In the present study, we developed an immersed boundary method (IB) for simulating fluid–flexible structure interactions. Our method is based on an efficient Navier-Stokes solver adopting the fractional step method and a staggered Cartesian grid system. The fluid motion defined on an Eulerian grid and the structure motion defined on a moving Lagrangian grid are independently solved, and their interaction is formulated using a momentum forcing. The proposed method was applied to simulating flow over flexible filaments with inextensibility constraint, and was then extended to simulate 3D flag motion in a uniform flow. Toward bio-mimetic applications, we also simulated a valveless pump and an energy harvesting eel by utilizing the 1D filament model, and a swimming jellyfish and a deformable disk by utilizing the 2D structure model.

1. Introduction

Systems involving flexible bodies interacting with surrounding fluid flow are commonplace – for example flapping flags and swimming fishes – and are becoming increasingly prevalent in biofluid engineering applications. Such phenomena are challenging to model numerically on account of their complex geometries and freely moving boundaries, which give rise to complicated fluid dynamics. In these systems, the flexible body acts on the surrounding fluid, forcing it to move with the moving boundary. On the other hand, the fluid exerts forces on the flexible body through pressure differences and viscous shear stresses. Together, these interactions between the fluid and the flexible-body can give rise to self-sustained oscillations such as the flapping of a flag. The fluid-flexible structure interaction is also an essential aspect of the tail and wing motions of swimming and flying animals. Even for active flapping motions such as those of swimming and flying animals, the flapping frequency cannot be selected arbitrarily (Wang 2000). Recent studies have disclosed a simple relationship between the flapping frequency, amplitude and forward speed for a wide range of species of animals to fly or swim with high propulsive efficiency (Triantafyllou et al. 2000; Taylor et al. 2003; Fish & Lauder 2006). Hence, study of the fluid-flexible structure interaction behavior sheds light on such biological processes. Moreover, it is of importance in areas such as paper engineering (Watanabe et al. 2002a, b), socio-medical conditions

(e.g., human snoring; Huang 1995), ocean/river power generation (Allen & Smits 2001; Taylor et al. 2001), and so on. In the present study, an IB method is developed for simulating fluid–flexible structure interactions.

2. Problem formulation

The incompressible viscous fluid flow is governed by the N-S equations and the continuity equation,

$$\rho_0 \left(\frac{\partial \mathbf{u}}{\partial t} + \mathbf{u} \cdot \nabla \mathbf{u} \right) = -\nabla p + \mu \nabla^2 \mathbf{u} + \mathbf{f}, \quad (1)$$

$$\nabla \cdot \mathbf{u} = 0, \quad (2)$$

where \mathbf{u} is the velocity vector, p is the pressure, ρ_0 is the fluid density, μ is the fluid dynamic viscosity, and \mathbf{f} is the momentum forcing applied to enforce the no-slip boundary condition along the IB.

The structure motion is defined on a moving Lagrangian grid. For a flexible filament described by a 1D curvilinear coordinate system, the equation of motion is written as

$$\rho_1 \frac{\partial^2 \mathbf{X}}{\partial t^2} = \frac{\partial}{\partial s} \left(\sigma \frac{\partial \mathbf{X}}{\partial s} \right) - \frac{\partial^2}{\partial s^2} \left(\gamma \frac{\partial^2 \mathbf{X}}{\partial s^2} \right) + \rho_1 \mathbf{g} - \mathbf{F}, \quad (3)$$

where s is the arclength, \mathbf{X} is the position, ρ_1 is density difference between the structure and the surrounding fluid, σ is the tension force along the filament axis, γ is the bending rigidity, \mathbf{F} is the Lagrangian forcing exerted on the filament by the surrounding fluid. For a

deformable surface defined on a 2D curvilinear coordinate system, which is moving in 2D or 3D fluid domain, the equation of motion is generalized as

$$\rho_1 \frac{\partial^2 \mathbf{X}}{\partial t^2} = \sum_{i,j=1}^2 \left[\frac{\partial}{\partial s_i} \left(\sigma_{ij} \frac{\partial \mathbf{X}}{\partial s_j} \right) - \frac{\partial^2}{\partial s_i \partial s_j} \left(\gamma_{ij} \frac{\partial^2 \mathbf{X}}{\partial s_i \partial s_j} \right) \right] + \rho_1 \mathbf{g} - \mathbf{F} \quad (4)$$

Since the Lagrangian grid passes across the fixed Eulerian grid as the structure moves in the fluid domain, the fluid-structure interaction is formulated through the momentum forcing. In the present study, we evaluate the momentum forcing at the Lagrangian points directly from the time-discretized equation of motion of the structure, i.e.

$$\mathbf{F}^n = -\frac{\tilde{\mathbf{X}}_{ib}^{n+1} - 2\mathbf{X}^n + \mathbf{X}^{n-1}}{\Delta t^2} + \mathbf{RHS}^{n+1}, \quad (5)$$

where \mathbf{RHS} regroups the elastic force terms and the gravity force term for simplicity, and $\tilde{\mathbf{X}}_{ib}^{n+1}$ represents an estimation of the new position of the fluid point. In computation, $\tilde{\mathbf{X}}_{ib}^{n+1}$ is estimated as

$$\tilde{\mathbf{X}}_{ib}^{n+1} = \mathbf{X}_{ib}^n + \mathbf{U}_{ib}^n \Delta t, \quad (6)$$

where \mathbf{X}_{ib}^n is the position of the fluid point at the present time step and \mathbf{U}_{ib}^n is the fluid velocity interpolated at the Lagrangian point \mathbf{X}^n . The velocity interpolation is expressed as

$$\mathbf{U}_{ib}^n(s_1, s_2, t) = \int_{\Omega} \mathbf{u}^n(\mathbf{x}, t) \delta(\mathbf{X}^n(s_1, s_2, t) - \mathbf{x}) d\mathbf{x}, \quad (7)$$

where δ denotes the Dirac delta function.

In practice, we found that the coefficient $-1/\Delta t^2$ in Eq.(5) becomes very large because Δt is usually given a small value. As a result, a stable solution may not be obtained. Hence, we adopt a relaxation of Eq.(5) as follows

$$\mathbf{F}^n = \kappa (\tilde{\mathbf{X}}_{ib}^{n+1} - 2\mathbf{X}^n + \mathbf{X}^{n-1}), \quad (8)$$

where κ is a large negative constant. After obtaining the Lagrangian momentum forcing term, we transform it to the Eulerian form using the Dirac delta function

$$\mathbf{f}^n(\mathbf{x}, t) = \int_{\Gamma} \mathbf{F}^n(\Gamma, t) \delta(\mathbf{x} - \mathbf{X}^n(\Gamma, t)) d\Gamma. \quad (9)$$

In the computations, the Eulerian momentum forcing is actually distributed across several grids in width according to the support of the smoothed approximation of the Dirac delta function (Peskin 2002).

3. Numerical method

The discretized N-S equations can be written as

$$\frac{\mathbf{u}^{n+1} - \mathbf{u}^n}{\Delta t} + \mathbf{N}\mathbf{u}^{n+1} = -Gp^{n+1/2} + \frac{1}{2\text{Re}} (\mathbf{L}\mathbf{u}^{n+1} + \mathbf{L}\mathbf{u}^n), \quad (10)$$

$$+ \mathbf{f}^n + \mathbf{mbc}$$

$$\mathbf{D}\mathbf{u}^{n+1} = 0 + \mathbf{cbc}, \quad (11)$$

where N , G , L and D are the linearized discrete convective operator, the discrete gradient operator, the discrete Laplacian operator, and the discrete divergence operator, respectively. The velocity boundary conditions for the momentum equations and the continuity equation have been imposed on \mathbf{mbc} and \mathbf{cbc} , respectively. In this study, we adopt the fractional step method to solve Eqs.(10) and (11) on a staggered Cartesian grid. The velocity components and momentum forcing are defined on the staggered grid, whereas the pressure is applied at the centers of cells. Fully implicit time advancement is employed, with the Crank-Nicholson scheme being used for the discretization of the diffusion and convection terms. Decoupling of the velocity and pressure is achieved by block LU decomposition in conjunction with approximate factorization (Kim et al. 2002).

We use the operator K to represent the discretized form of the elastic force, i.e.,

$$\mathbf{F}_e = K\mathbf{X}. \quad (12)$$

The discretized form of the equation of structure motion is then written as

$$\frac{\mathbf{X}^{n+1} - 2\mathbf{X}^n + \mathbf{X}^{n-1}}{\Delta t^2} = K\mathbf{X}^{n+1} + \text{Fr} \frac{\mathbf{g}}{g} - \mathbf{F}^n + \mathbf{BC}, \quad (13)$$

where the elastic force term is treated implicitly, the momentum forcing term \mathbf{F}^n is calculated using Eq.(8), and the last term, \mathbf{BC} , is the boundary condition vector which contains the known positions at the fixed boundary. After rearrangement, Eq.(13) becomes

$$\mathbf{A}\mathbf{X}^{n+1} = \mathbf{R}^n. \quad (14)$$

Here $\mathbf{A} = \mathbf{I} - \Delta t^2 K$, where \mathbf{I} is the unit matrix, and $\mathbf{R}^n \equiv \mathbf{X}^n + \Delta t \mathbf{U}^{n-1} + \Delta t^2 \text{Fr} \cdot \mathbf{g}/g - \Delta t^2 \mathbf{F}^n + \Delta t^2 \mathbf{BC}$ by applying $\mathbf{U}^n = (\mathbf{X}^n - \mathbf{X}^{n-1})/\Delta t$. To solve Eq.(14), we need to know the initial position and velocity of the flag. We found that symmetry and positive-definiteness of the matrix \mathbf{A} are preserved in this study. Hence, the conjugate gradient method can be utilized to solve Eq.(14) in an efficient manner due to its fast convergence rate.

The overall process of the present numerical algorithm is summarized as follows:

- (1) At the n th time step, we know the fluid velocity field and the structure position \mathbf{X}_n and velocity \mathbf{U}_n . Estimate the new position of the fluid point. Then calculate the Lagrangian momentum forcing \mathbf{F}^n using Eq.(8).
- (2) Spread the Lagrangian momentum forcing to the Eulerian grid using Eq.(9). Solve Eqs.(10) and (11) to obtain the updated fluid velocity field and pressure field. Interpolate the fluid velocity at the IB and calculate the new position of the fluid point.
- (3) Substitute \mathbf{F}^n into Eq.(14) and solve this equation to obtain the structure position at the new time step, as well as the structure velocity, i.e. $\mathbf{U}^{n+1} = (\mathbf{X}^{n+1} - \mathbf{X}^n)/\Delta t$. This ends one time step marching.

4. Numerical results

4.1. Flow over a flexible filament

When a flexible filament is placed in a uniform flow, the computational domain is $-2 \leq x \leq 6$ and $-4 \leq y \leq 4$. The filament is simply supported at its leading edge and is free at its trailing edge. The inextensibility condition is applied when solving the filament motion equation, i.e.

$$\frac{\partial \mathbf{X}}{\partial s} \cdot \frac{\partial \mathbf{X}}{\partial s} = 1. \quad (15)$$

Fig.1 shows the instantaneous vorticity contours over a filament for $Re=200$ and $\gamma=0.001$ at four instants that approximately span a flapping period, i.e. $t=9.2, 10.0, 10.8$ and 11.6 . The filament achieves a self-sustained flapping state, and symmetric vortices are shed alternately from the free end at the moment when it is most bent. When we increase Re to 500 and decrease γ to 0.0001, two positive and two negative vortices are shed sequentially from the filament, as shown in Fig.2. In this system each vortex is split into two small vortices by the bending of the free end. We can see that the production of a small vortex procession is a combined effect of the Reynolds number and bending rigidity. Interestingly, a previous study of the flow around a swimming eel also observed that two same-sign vortices were shed per tail beat (Müller et al. 2001; Tytell et al. 2004).

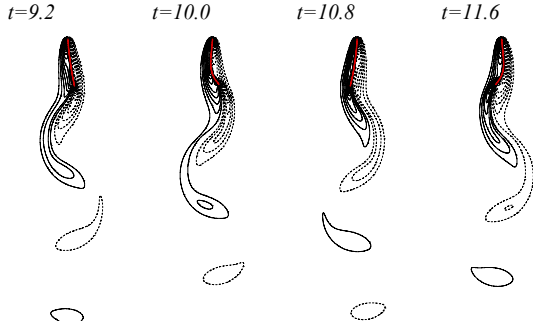


Fig.1 Instantaneous vorticity contours of a uniform flow over a filament for $Re=200$ and $\gamma=0.001$.

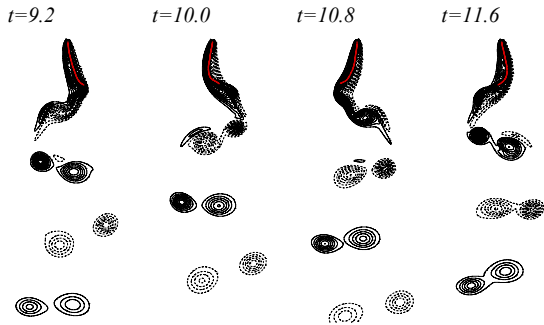


Fig.2 Instantaneous vorticity contours of a uniform flow over a filament for $Re=500$ and $\gamma=0.0001$.

To study the bistable property of the present system, we consider both $L=0.5$ and $L=1.0$. The node numbers along the filament (N) for these systems are 64 and 32, respectively. The behaviors of filaments with simply supported ($BC1$) and clamped ($BC2$) boundary conditions at the fixed end are compared. For the short filament (Fig.3a), by setting a large initial disturbance $a=0.03$, self-sustained flapping eventually develops for

both $BC1$ and $BC2$, although the filament with $BC2$ requires a longer time to reach the equilibrium state. On the other hand, by setting a small value of $a=0.01$, the initial disturbance decays gradually and the filament comes to rest at the stretched-straight state. For a small initial disturbance, the motion is mostly limited to the region close to the free end; hence there is little difference between $BC1$ and $BC2$ in Fig.3a when the motion is decaying. For the longer filament (Fig.3b), a self-sustained flapping state quickly develops for both $BC1$ and $BC2$ with an initial disturbance $a=0.01$, and slowly develops for a small initial disturbance $a=0.001$. In all of our simulations of filaments of length $L=1.0$, the flapping state eventually developed no matter how small the initial disturbance. This is consistent with the experimental finding that the stable stretched-straight state disappears and only the flapping state remains if L is sufficiently large (Zhang et al. 2000). More results on flow over flexible filaments have been presented in Huang et al. (2007).

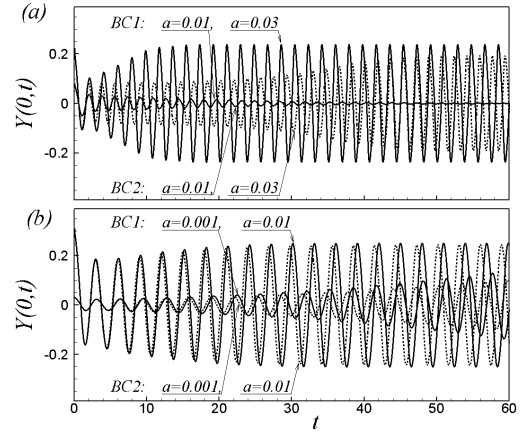


Fig.3 Time history of the free end position of the filament with (a) $L=0.5$; (b) $L=1.0$.

4.2. A flapping flag in a uniform flow

In the present simulations, the computational domain for fluid flow is a 3D rectangular box, extending from $(-1, -4, -1)$ to $(7, 4, 1)$ in the streamwise (x), transverse (y) and spanwise (z) directions, respectively. The fixed boundary of the flag ($s_1=0$) is aligned with the z -axis, and the flow is coming along the x -axis. The flag is initially held at an angle of $a=0.1\pi$ from the xz plane. Fig.4 shows instantaneous flag positions during a flapping period at $Re=500$ and $Fr=0$. At $t=16.86$ and 18.54 , the trailing edge reaches its maximum transverse position, while at $t=17.94$ and 19.68 we can see that a wave is traveling along the longitudinal (s_1) direction. Small wavy motions are apparent on the flag surface, although the main wave remains uniform in the s_2 -direction. As shown in Fig.5, vortex rings are formed behind the flag. Interestingly, the vortex shedding from the trailing edge forms an O-shaped structure, while that from the side edges forms a Ω -shaped structure that is connected to the O-shaped structure at the bottom.

Then we take into account the effects of the gravity force. The direction of the gravity force is along the

spanwise (z) direction, i.e. $\mathbf{g}/|\mathbf{g}|=(0,0,-1)$. We use $Re=500$ and $Fr=0.2$ in this simulation. Fig.6 shows instantaneous images of the flag positions at four time instants. It is shown that the flag is sagging down at $t=15.60$, and the upper corner of the trailing edge undergoes a fast rolling motion near the maximum or minimum transverse position from $t=13.98$ to 14.46. The instantaneous 3D vortical structures around the flag are shown in Fig.7. The O-shaped structures are still evident, whereas the Ω -shaped structures are disrupted due to the sagging-down of the flag and the fast rolling of its upper corner.

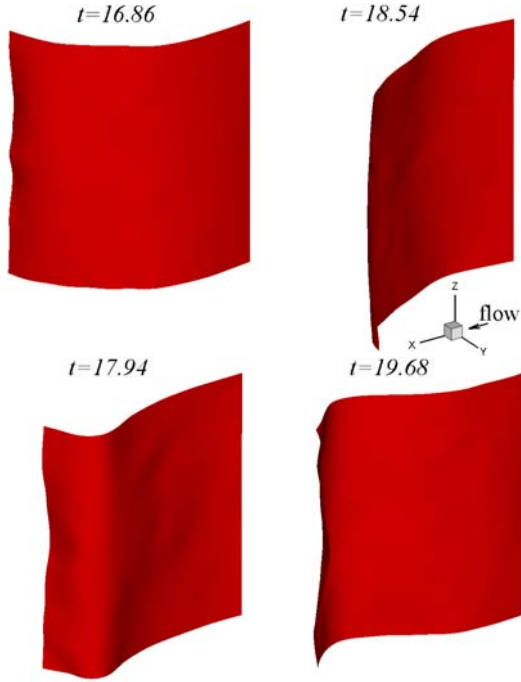


Fig.4 Instantaneous positions of a flapping flag at $Re=500$ and $Fr=0$.

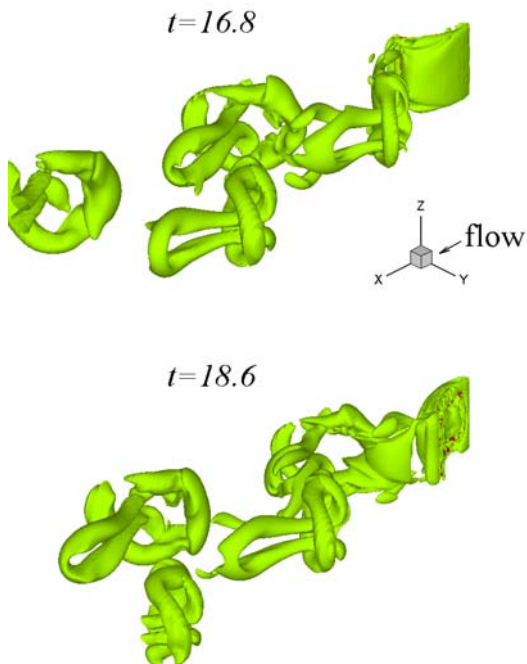


Fig.5 Vortical structures shedding from the flapping flag at $Re=500$ and $Fr=0$.

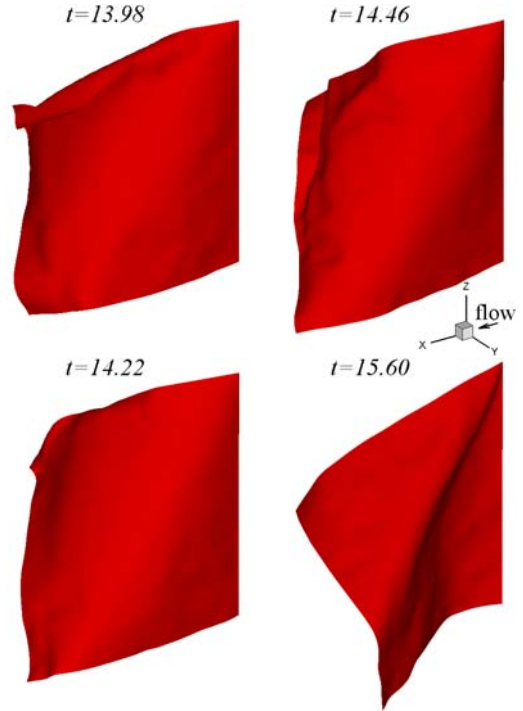


Fig.6 Instantaneous positions of a flapping flag at $Re=500$ and $Fr=0.2$.

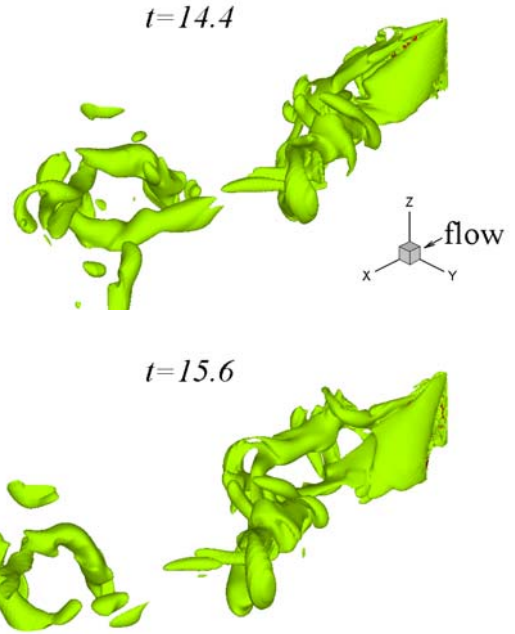


Fig.7 Vortical structures shedding from the flapping flag at $Re=500$ and $Fr=0.2$.

4.3. A swimming jellyfish

Similar with Zhao et al. (2008), a 2D model of jellyfish is shown in Fig.8. The initial top and bottom surfaces are described by

$$X^0(s) = (\gamma s, \beta - \alpha(\gamma s)^2 - \eta(\gamma s)^4), \quad (16)$$

where $\alpha=0.03$, $\beta=1.0$, $\gamma=2.6$, $\eta=0.05$ for the top and $\alpha=0.02$, $\beta=0.2$, $\gamma=2.45$, $\eta=0.045$ for the bottom. A stretched grid is adopted, i.e. $s=\tanh(\lambda s^0)/\tanh(s^0)$ for $-1 \leq s^0 \leq 1$, where $\lambda=1.8$ for the top and $\lambda=1.5$ for the

bottom. As a result, the grid is distributed more closely at the tips.

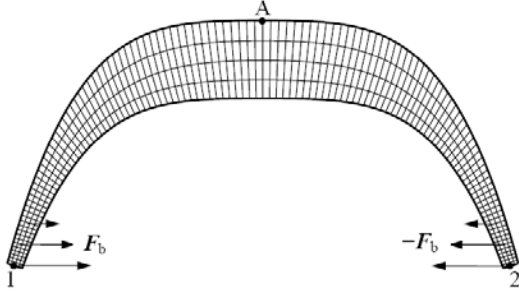


Fig.8 The Lagrangian grid for a two-dimensional jellyfish at the initial stage.

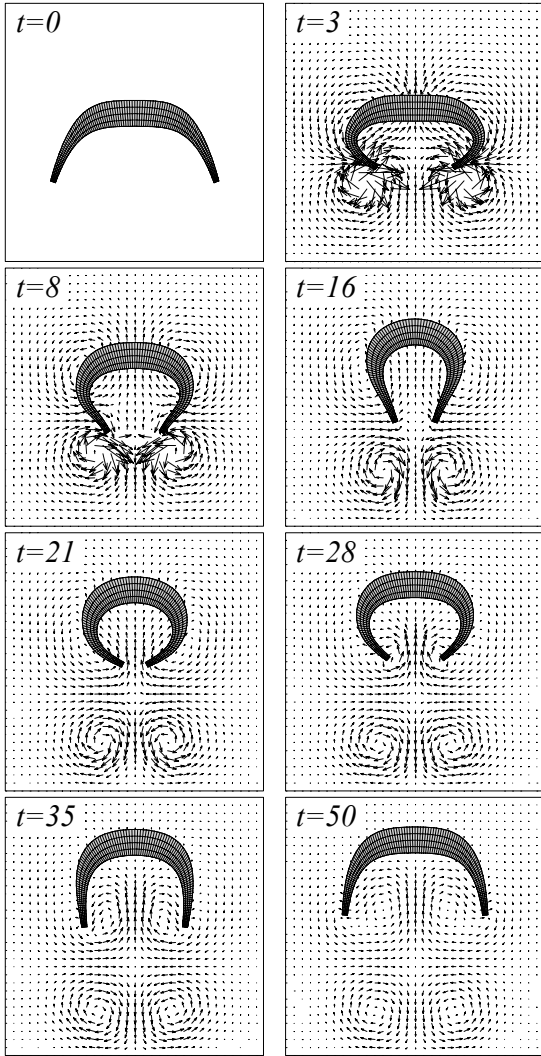


Fig.9 Swimming of a jellyfish at $Re=300$: velocity field and jellyfish positions.

The jellyfish is moving forward by contracting and relaxing its body repeatedly. The body force in a period is modeled by

$$F_b = \begin{cases} (2-r) \min(t, 4-t) \frac{X_{21}}{|X_{21}|}, & r < 2, t < 4 \\ 0, & \text{otherwise} \end{cases}, \quad (17)$$

where r denotes the distance between the force point and the left tip, and X_{21} denotes the vector pointed from the force point to its symmetric counterpart. Eq.(17) indicates that the body force is only exerted near the tips and at the beginning stage of each period, which is 50 in this simulation.

The flow domain is a 4×4 box where the no-slip condition is applied at all the four boundaries. Fig.9 shows the body positions of a swimming jellyfish and the induced flow field at $Re=300$. Since the density of jellyfish is close to its surrounding fluid, we use a small density difference, $\rho_1/\rho_0=0.1$, and the gravity force is neglected in this simulation. At the beginning stage, the jellyfish is deformed fast due to the body force, and a vortex ring is formed near the tips. Then the body is contracting by the inertial force, and the vortex ring is ejected from the tips, which push the body to move forward. After the two tips reach their maximum deformation, the body begins relaxation, and a reversed vortex ring is formed between the tips, which is much weaker than the first one. During the relaxation phase, the body is still moving forward by the inertial force.

The effect of density ratio, $\rho = \rho_1/\rho_0$, is evaluated in Fig.10, which shows time histories of the forward velocity of point A (see Fig.8). The curves for different ρ have similar shapes, but that of large ρ lags more due to the inertial force. When $\rho \leq 0.1$, the curves are collapsed, indicating that the results for sufficient small ρ are converged to that of the neutral buoyant case.

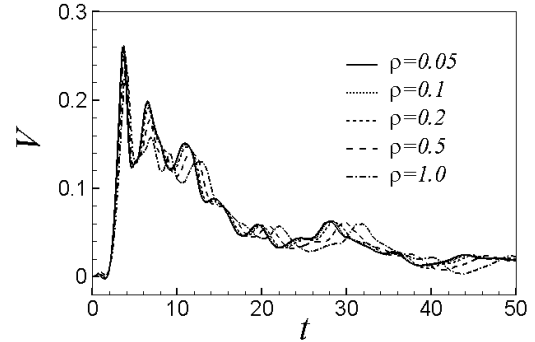


Fig.10 Time history of the forward velocity of point A (marked in Fig.8) for different structure densities.

4.4. A deformable ring moving through a channel with contraction

The initial shape of a deformable ring is circular, and the grid distribution is shown in Fig.11. The radii of the inner and outer circles are denoted by r_i and r_o , respectively, and the thickness, $a = r_o - r_i$, is 0.2 in this simulation, which is scaled by the diameter of the outer circle. The ring interacts with the fluid only along its outer edge, while the inner edge is developing freely. In the peripheral direction, a periodic boundary condition is adopted.

The channel has a length of 16 in the streamwise direction and a width of 2 in the normal direction. At the middle of channel, there are half-circle rigid obstacles on the upper and lower walls, both of which have radii of 0.6. A flow with a parabolic velocity profile is given as the initial flow field. The no-slip

conditions on the contraction surfaces and the outer edge of the deformable ring are satisfied by the IB method.

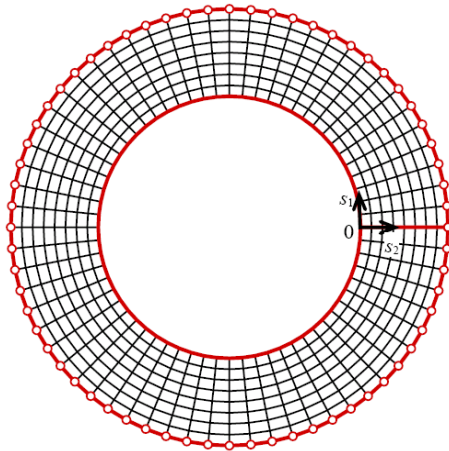


Fig.11 The Lagrangian grid for a deformable ring at the initial stage.

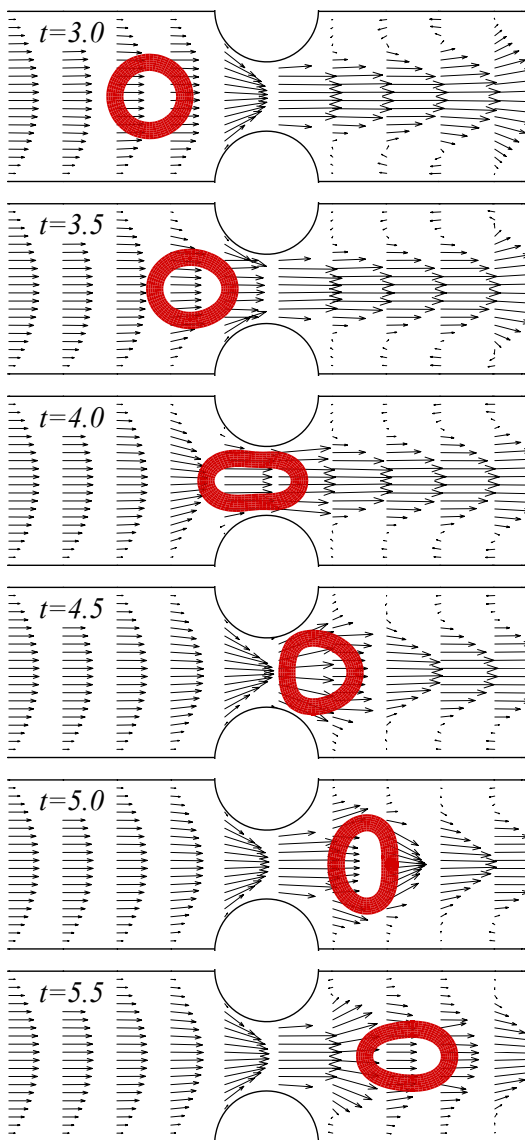


Fig.12 A deformable ring moving through a channel with contraction at $Re=100$: velocity field and ring positions.

Fig.12 shows the instantaneous velocity field and the ring positions at $Re=100$. Before encountering the contraction part, the ring moves by following the fluid flow with slight deformation. It is then compressed due to the lubrication force when moving through the contraction part, without contacting with the rigid walls. After passing the contraction part, the ring is relaxed with elastic oscillations, which decay faster at lower Reynolds numbers.

5. Conclusions

Systems involving flexible bodies interacting with surrounding fluid flow are not only commonplace in our daily life but also of significance in engineering. In the present study, we developed an IB method for simulating fluid-flexible structure interactions. The proposed IB method is based on an efficient Navier-Stokes solver adopting the fractional step method and a staggered Cartesian grid system. The fluid motion defined on an Eulerian grid and the structure motion defined on a moving Lagrangian grid are independently solved, and their interaction is formulated using a momentum forcing. Transformation between the Lagrangian and Eulerian variables is realized using a smoothed Dirac delta function.

The proposed method was first applied to simulating a uniform flow around a flexible filament with inextensibility constraint. The mechanism by which small vortex processes are produced was attributed to the increase of Reynolds number and the decrease of bending rigidity. The bistable property of the system was observed by altering the filament length. Next, we extended our method for the 3D simulation of a flapping flag in a uniform flow. The flag motion equation was derived using the energy method. When the gravity force is excluded, the flag flaps almost uniformly along the spanwise direction, with an O-shaped vortical structure shedding from the trailing edge connected by a Ω -shaped structure shedding from both side edges. When the gravity force is included, the resulting sagging-down of the flag and rolling-up of the upper-corner deform the vortical structures.

Toward bio-mimetic applications, we simulated a swimming jellyfish. Contraction of the body produces and ejects a vortex ring, which push the body to move forward. The effect of density difference was investigated. It is shown that results for sufficient small density difference are converged to that of the neutral buoyant case. A deformable ring moving through a channel with contraction was then simulated. The ring is compressed by the contraction part due to the lubrication force, and is relaxed with elastic oscillations after passing the contraction part.

Beside the above examples, we have simulated several other problems, e.g. multiple filaments in side-by-side and tandem alignments, a deformable loop as a 2D body, a valveless pump and an energy harvesting eel. Moreover, results on both 2D and 3D numerical models of the aortic valve will be also presented in the lecture.

Acknowledgements

This work was supported by the Acceleration Research of the Korea Science & Engineering Foundation and partially supported by the Korea Institute of Science and Technology Information under the Strategic Supercomputing Support Program.

References

- Allen, J. J. & Smits, A. J., 2001 Energy Harvesting Eel. *J. Fluids Struct.* Vol.15, pp.629-640.
- Fish, F. E. & Lauder, G. V., 2006 Passive and Active Flow Control by Swimming Fishes and Mammals. *Annu. Rev. Fluid Mech.*, Vol.38, pp.193-224.
- Huang, L., 1995 Flutter of cantilevered in axial flow. *J. Fluids Struct.*, Vol.9, pp.127-147.
- Huang, W.-X., Shin, S. J. & Sung, H. J., 2007 Simulation of Flexible Filaments in a Uniform Flow by the Immersed Boundary Method. *J. Comput. Phys.*, Vol.226, pp.2206-2228.
- Kim, K., Baek, S.-J. & Sung, H. J., 2002 An implicit velocity decoupling procedure for incompressible Navier-Stokes equations. *Int. J. Numer. Meth. Fluids*, Vol.38, pp.125-138.
- Müller, U. K., Smit, J., Stamhuis, E. J. & Videler, J. J., 2001 How the Body Contribute to the Wake in Undulatory Fish Swimming: Flow Fields of a Swimming Eel (*Anguilla Anguilla*). *The Journal of Experimental Biology*, Vol.204, pp.2751-2762.
- Peskin, C. S., 2002 The immersed boundary method. *Acta Numerica*, pp.479-517.
- Taylor, G. K., Nudds, R. L. & Thomas, A. L. R., 2003 Flying and swimming animals cruise at a Strouhal number tuned for high power efficiency. *Nature*, Vol.425, pp.707-711.
- Taylor, G. W., Burns, J. R., Kammann, S. M., Powers, W. B. & Welsh, T. R., 2001 The Energy Harvesting Eel: A Small Subsurface Ocean/River Power Generator. *IEEE Journal of Oceanic Engineering*, Vol.26(4), pp.539-547.
- Triantafyllou, M. S., Triantafyllou, G. S. & Yue, D. K. P., 2000 Hydrodynamics of Fishlike Swimming. *Annu. Rev. Fluid Mech.*, Vol.32, pp.33-53.
- Tytell, E. D. & Lauder, G. V. 2004 The hydrodynamics of eel swimming I. Wake structure, *The Journal of Experimental Biology*, Vol.207, pp.1825-1841.
- Wang, Z. J., 2000 Vortex shedding and frequency selection in flapping flight. *J. Fluid Mech.*, Vol.410, pp.323-341.
- Watanabe, Y., Suzuki, S., Sugihara, M. & Sueoka, Y., 2002a An experimental study of paper flutter. *J. Fluids Struct.* Vol.16, pp.529-542.
- Watanabe, Y., Isogai, K., Suzuki, S. & Sugihara, M., 2002b A theoretical study of paper flutter. *J. Fluids Struct.* Vol.16, pp.543-560.
- Zhang, J., Childress, S., Libchaber, A. & Shelley, M., 2000 Flexible filaments in a flowing soap film as a model for one-dimensional flags in a two-dimensional wind. *Nature*, Vol.408, pp.835-839.
- Zhao, H., Freund, J. B. & Moser, R. D., 2008 A fixed-mesh method for incompressible fluid-

structure systems with finite solid deformations. *J. Comput. Phys.*, Vol.227, pp.3114-3140.